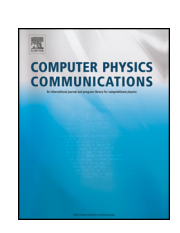
FISEVIER

Contents lists available at ScienceDirect

Computer Physics Communications

journal homepage: www.elsevier.com/locate/cpc



Computational Physics

Band unfolding with a general transformation matrix: From code implementation to interpretation of photoemission spectra *



Oleg Rubel^{a,*}, Jean-Baptiste Moussy^b, Paul Foulquier^{b,c}, Véronique Brouet^{c,*}

- a Department of Materials Science and Engineering, McMaster University, 1280 Main Street West, Hamilton, Ontario L8S 4L8, Canada
- b Université Paris-Saclay, CEA, CNRS, SPEC, 91191, Gif-sur-Yvette, France
- ^c Université Paris-Saclay, CNRS, Laboratoire de Physique des Solides, 91405, Orsay, France

ARTICLE INFO

Article history: Received 6 January 2023 Received in revised form 15 May 2023 Accepted 21 May 2023 Available online 8 June 2023

Keywords:
Band structure
Density functional theory
Supercell
Angle-resolved photoemission spectroscopy
Spectral function

ABSTRACT

Unfolding of a supercell band structure into a primitive Brillouin zone is important for understanding implications of structural distortions, disorder, defects, and solid solutions on materials electronic structure. The necessity of band unfolding is also recognized in the interpretation of angle-resolved photoemission spectroscopy (ARPES) measurements. We describe an extension of the fold2Bloch package by implementing an arbitrary transformation matrix used to establish a relation between the primitive cell and supercell. This development allows us to overcome limitations of supercells constructed exclusively by scaling of primitive cell lattice vectors. It becomes possible to transform between primitive and conventional cells as well as include rotations. The fold2Bloch is publicly available from a GitHub repository as a FORTRAN code. It interfaces with the all-electron full-potential WIEN2k and the pseudopotential VASP density functional theory packages. The fold2Bloch is supplemented by additional pre- and post-processing utilities that aid in generating k points in the supercell (such that they later fall onto a desired path in the primitive Brillouin zone after unfolding) and plotting the unfolded band structure. We selected Sr₂IrO₄ as an illustrative example and, for the first time, present its properly unfolded band structure in direct comparison with ARPES measurements. In addition, critical importance of the band unfolding for interpretation of SrIrO₃ ARPES data is illustrated and discussed as a perspective.

© 2023 Elsevier B.V. All rights reserved.

1. Introduction

The band dispersion E(k) obtained from electronic structure calculations provides information about the Fermi surface of metals, direct/indirect transition in semiconductors, effective masses, etc. When periodicity is perturbed (e.g., solid solutions, defects, magnetic order) the Brillouin zone (BZ) shrinks and bands get folded. As a result, E(k) becomes obscured and difficult to interpret.

Even when the periodicity is formally perturbed, it is still possible to recover an effective band structure in a BZ of the primitive cell using a k-spectral decomposition also known as 'band unfolding'. There are numerous examples of band unfolding. The notable milestones include an electronic structure of aperiodic solids [1–3], solid solutions described within a tight-binding approxima-

 $\label{lem:condition} \textit{E-mail addresses: } rubelo@mcmaster.ca \ (O. \ Rubel), \ veronique.brouet@u-psud.fr \ (V. \ Brouet).$

tion [4–6] or pseudopotentials with a plane-wave basis set [7–9], and Wannier functions derived from first-principle calculations to interpret angle-resolved photoemission spectroscopy (ARPES) experiments [10]. There are a number of public implementations of band unfolding in the density functional theory (DFT) community, for instance, BandsUP [11,12], fold2Bloch [13], VASPKIT [14], and vaspwfc [15].

The simplest scenario to unfold the band structure involves the supercell constructed from primitive real-space lattice vectors \mathbf{a}_i (i=1,2,3) by scaling them with an integer $n_i\mathbf{a}_i$ ($n_i\in\mathbb{Z}^+$). However, this does not cover all possibilities. There are lattices constructed by a combination of rotation and scaling of the primitive structural unit. Examples include a conventional vs reduced unit cell [16,17] or an octahedral rotation and tilting in perovskite structures [18].

Popescu and Zunger [9] suggested a more general approach to unfolding that involves a transformation matrix. It was already implemented in BandsUP, VASPKIT, and vaspwfc but not in fold2Bloch.

The review of this paper was arranged by Prof. Blum Volker.

^{*} Corresponding authors.

2. Methods

2.1. Lattice transformations

Following the notations in Ref. [9] we denote by lower-case (upper-case) symbols quantities referring to the primitive cell (supercell). Transformation of real-space primitive \mathbf{a}_i to supercell \mathbf{A}_i lattice vectors can be expressed as [19]

$$\mathbf{A}_{i} = \sum_{i=1}^{3} P_{ji} \, \mathbf{a}_{j} \quad (i = 1, 2, 3)$$
 (1)

or in the matrix form as

$$A = P^{\mathsf{T}} a, \tag{2}$$

where the lattice vectors matrices A and a are constructed of rows being individual vectors and columns being their Cartesian components (x, y, z), e.g.,

$$A = \begin{pmatrix} \mathbf{A}_1 \\ \mathbf{A}_2 \\ \mathbf{A}_3 \end{pmatrix} \equiv \begin{bmatrix} A_{11} & A_{12} & A_{13} \\ A_{21} & A_{22} & A_{23} \\ A_{31} & A_{32} & A_{33} \end{bmatrix}. \tag{3}$$

Here P is a transformation matrix of the size 3×3 compatible with conventions recommended by the International tables for crystallography [19] (same as in VESTA structure visualization software [20] or Bilbao crystallographic server [21] but different from Ref. [9]). The transformation matrix is obtained by solving the linear Eq. (2), which yields

$$P = (Aa^{-1})^{\mathsf{T}}. (4)$$

The reverse transformation of a supercell to the primitive cell is obtained using the inverse matrix P^{-1}

$$a = (P^{-1})^{\mathsf{T}} A. \tag{5}$$

Scaling of the cell volume as a result of the primitive cell to supercell transformation is given by [19]

$$n_{v} = \det(P), \tag{6}$$

which imposes two requirements: P should be positive defined and $P_{ij} \in \mathbb{Z}$, from which it follows that $\det(P) \in \mathbb{Z}^+$. These requirements translate into a right-handed set of vectors. The code will stop with an error if a negative determinant is encountered.

Reciprocal lattice vectors are also transformed using P. Owing to the relation $B = (A^{-1})^{\mathsf{T}}$, reciprocal lattice vectors of a supercell \mathbf{B}_i can be transformed to the reciprocal primitive vectors \mathbf{b}_i as [19]

$$b = P B \tag{7}$$

and back as

$$B = P^{-1}b. (8)$$

Note that the transposition of P is not required for converting reciprocal lattice vectors in the matrix form contrary to the conversions proposed in Ref. [9] (see Eqs. (1) and (2) therein).

2.2. Band unfolding

We outlined in Ref. [13] an unfolding procedure used in the fold2Bloch implementation when a supercell is constructed by simple scaling of the primitive cell. Here we present an extended (more general) version.

DFT codes for solids internally operate with wave vectors in fractional coordinates. Here we will use tilde to denote primitive

(supercell) fractional coordinates $\tilde{\mathbf{k}}$ ($\tilde{\mathbf{K}}$) where components of each vector span a range between 0 and 1. Cartesian components of the wave vector are obtained by a multiplication with the reciprocal lattice matrix

$$\mathbf{k} = \tilde{\mathbf{k}} b \tag{9}$$

and similarly for the supercell K.

Transformation of reciprocal-space supercell $\tilde{\mathbf{k}}$ to primitive $\tilde{\mathbf{k}}$ wave vectors (fractional coordinates) is given by [19]

$$\tilde{\mathbf{k}} = [\tilde{\mathbf{K}} + (m_1, m_2, m_3)] P^{-1} \mod 1.$$
 (10)

With all possible combinations of $m_i \in \mathbb{Z}$, the number of unique \mathbf{k} points generated within the first BZ of the primitive cell (Fig. 1) is given by the volume scale (Eq. (6)). The new (unfolded) k points in Fig. 1b form two subsets \mathbf{k}_1 (open markers) and \mathbf{k}_2 (red) of the original grid $\mathbf{K} + \mathbf{G}$ in Fig. 1a. The two subsets were created since the volume change is $n_v = 2$ in the example shown. More generally, the subset property is expressed as

$$\mathbf{k}_l + \mathbf{g} \subset \mathbf{K} + \mathbf{G} \quad (l = 1, \dots, n_{\mathsf{V}}), \tag{11}$$

with $\mathbf{G}(m_1, m_2, m_3) = m_1\mathbf{B}_1 + m_2\mathbf{B}_2 + m_3\mathbf{B}_3$ and $\mathbf{g}(m_1, m_2, m_3) = m_1\mathbf{b}_1 + m_2\mathbf{b}_2 + m_3\mathbf{b}_3$ being commensurate vectors of the plane wave expansion.

The wave function in WIEN2k is split into two regions: the atomic spheres and the interstitial region [22,23]. A plane wave basis set is used in the interstitial region

$$\Psi_{\sigma,n,\mathbf{K}}^{(\text{int})}(\mathbf{r}) = \sum_{\mathbf{r}} C_{\sigma,n,\mathbf{K}}(\mathbf{G}) e^{i(\mathbf{K}+\mathbf{G})\cdot\mathbf{r}},$$
(12)

where C are plane wave coefficients for a specific electronic state with the wave vector \mathbf{K} , spin channel σ , band index n. Plane waves are also used in the Vienna *ab initio* simulation package (VASP) [24] to construct pseudo wave functions in the framework of a projector augmented-wave method [25,26].

Spectral weight of the new unfolded k point is evaluated from the subset of plane wave coefficients [9]

$$w_{\sigma,n}(\mathbf{k}_l) = \sum_{\mathbf{g}} |C_{\sigma,n,\mathbf{K}}(\mathbf{k}_l + \mathbf{g})|^2 \quad (l = 1, \dots, n_{\mathbf{v}}). \tag{13}$$

Weights of each spin component are normalized such that

$$\sum_{l=1}^{n_{V}} w_{\sigma,n}(\mathbf{k}_{l}) = 1. \tag{14}$$

In the case of a spinor wave function in fold2Bloch for WIEN2k, weights of spin up and down components are mixed

$$w_n(\mathbf{k}) = \alpha^2 w_{\uparrow,n}(\mathbf{k}) + \beta^2 w_{\downarrow,n}(\mathbf{k}), \tag{15}$$

where α and β are components of the spinor wave function $(\alpha^2 + \beta^2 = 1)$ calculated by WIEN2k and stored in case.normso (up/dn) files. For a spinor wave function in fold2Bloch for VASP, weights of both spin channels are added following a scheme proposed by Medeiros et al. [12] using the normalization

$$\sum_{l=1}^{n_{\mathsf{v}}} \sum_{\sigma} w_{\sigma,n}(\mathbf{k}_l) = 1. \tag{16}$$

The α and β components are not explicitly calculated for VASP, since they are included in the weights.

We would like to note that WIEN2k is not a unique all-electron full potential codes that are capable of unfolding a band structure.

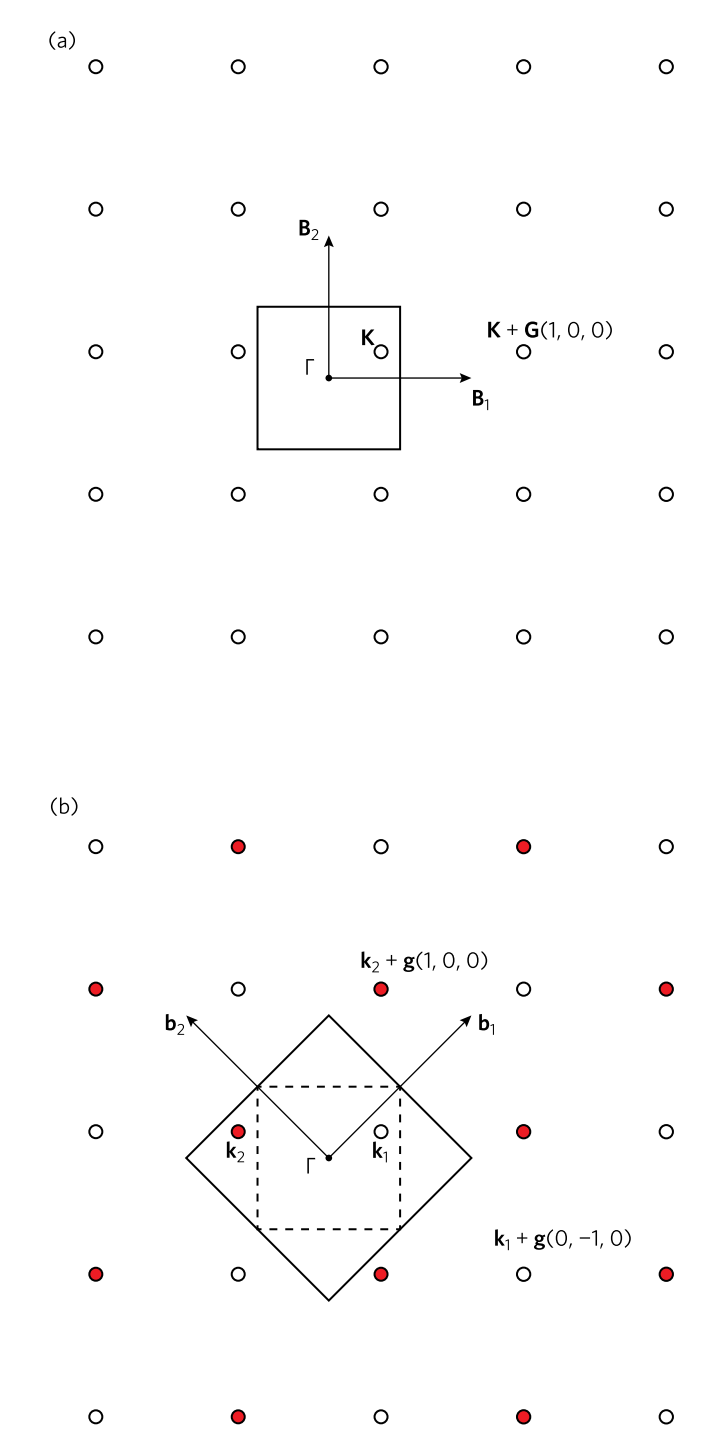


Fig. 1. Unfolding in reciprocal space. (a) BZ of a supercell with an arbitrary **K** point. (b) BZ of a primitive cell obtained by the two-dimensional transformation matrix of $P = [1, 1; \bar{1}, 1]$. The cell volume doubles $(n_v = 2)$, thus the **K** point transforms into two new point \mathbf{k}_1 and \mathbf{k}_2 that form two groups of plane wave coefficients (open and red markers). The dashed line shows the supercell BZ inside of the primitive BZ

There are other codes in that family, e.g., FLEUR [27], which includes the full transformation matrix. The unfolding method is not limited to plane waves. Other basis sets can also be used, e.g., localized basis sets (see references in Sec. 1 related to the tight-binding approximation). In general, the band unfolding is equivalent to construction of 'diffraction patterns' for each electronic eigenstate based on $\Psi_{\sigma,n,[\mathbf{K}]}(\mathbf{r})$ rather than the electron density (or potential) as in the case of traditional x-ray (or electron) diffraction. Here the square brackets $[\mathbf{K}]$ indicate that the wave function

Table 1 Structural and calculation parameters.

Parameters	Sr ₂ IrO ₄	SrIrO ₃
Space group (non-magnetic)	88 (I4 ₁ /a)	62 (Pbnm)
Space group (magnetic)	13 (P2/c)	n/a
Lattice param. (Å)	5.485, 25.775	5.568, 5.597, 7.892
R _{MT} (bohr)	2.24 (Sr)	2.26 (Sr)
	1.98 (Ir)	2.09 (Ir)
	1.62 (0)	1.71 (0)
$n_{\rm val}$	10 (Sr)	10 (Sr)
	31 (Ir)	31 (Ir)
	2 (0)	2 (0)
$R_{\text{MT}_{\text{min}}} K_{\text{max}}$	7.0	7.0
G_{\max}	12	12
l _{max}	10	10
$l_{ m vns}_{ m max}$	6	4
k mesh	$12 \times 12 \times 2$	$11 \times 11 \times 7$
	(shifted)	
Energy (Ry) and	10^{-4}	10^{-4}
charge converg.	10^{-3}	10^{-3}

should not necessarily have a wave vector associated with a supercell BZ. Even aperiodic solids have a diffraction pattern, which allows to infer a diffuse spectral function $A(E, \mathbf{k})$, at least for states dominated by long wavelengths, even if we cannot define a BZ (see related references in Sec. 1).

2.3. Electronic structure calculations

All electronic structure calculations were performed with WIEN2k DFT package [22,23]. Relevant parameters are listed in Table 1. We used the Perdew, Burke, and Ernzerhof [28] (PBE) exchange-correlation functional in combination with the onsite Hubbard correction U [29] for Ir-d electrons in the case of $\mathrm{Sr_2IrO_4}$. The spin-orbit coupling (SOC) was included in all calculations. The spin polarization was enabled only in the case of $\mathrm{Sr_2IrO_4}$, where we used a collinear antiferromagnetic ordering as in Ref. [30] (Fig. 2d) initialized with the magnetic moment of ± 1 Bohr magneton ($\mu_{\rm B}$) per Ir site.

2.4. Implementation and execution workflow

The fold2Bloch is available from GitHub as two repositories [31,32] for WIEN2k and for VASP DFT packages. Each repository contains the main source code written in FORTRAN as well as preand post-processing utilities. The utilities are designed to assist with k point generation on a desired path in a folded/unfolded BZ and plotting unfolded band structures (the spectral weights as a function of E and E). Implementation of the new functionality described in this article required changes in ca. 10-20% of the code. Changes mostly affected subroutines responsible for generating the new unfolded E points in the primitive cell [files NewK.f90 (WIEN2k) and kgen_prim.f90 (VASP)]. Changes in input arguments (the full matrix E instead of the number of folds along each reciprocal lattice vector) required modifications in the main program fold2Bloch.F90, as well as in pre- and post-processing utilities.

WIEN2k: First we initialize the calculation and complete the self-consistent field (SCF) cycle using the case.struct structure file as an input to obtain a self-consistent potential and a charge density. Once the calculation converges all necessary files are saves in the SOC folder. A detailed workflow can be found in Zenodo repository [33].

VASP: Complete a standard SCF calculation to generate a self-consistent charge density file CHGCAR.

Utils/fold.m: Next we generate a list of *folded* $\tilde{\mathbf{K}}$ points within the supercell BZ using the Octave/MATLAB script that takes a desired $\tilde{\mathbf{k}}$ point path in the primitive BZ, the number of intermediate

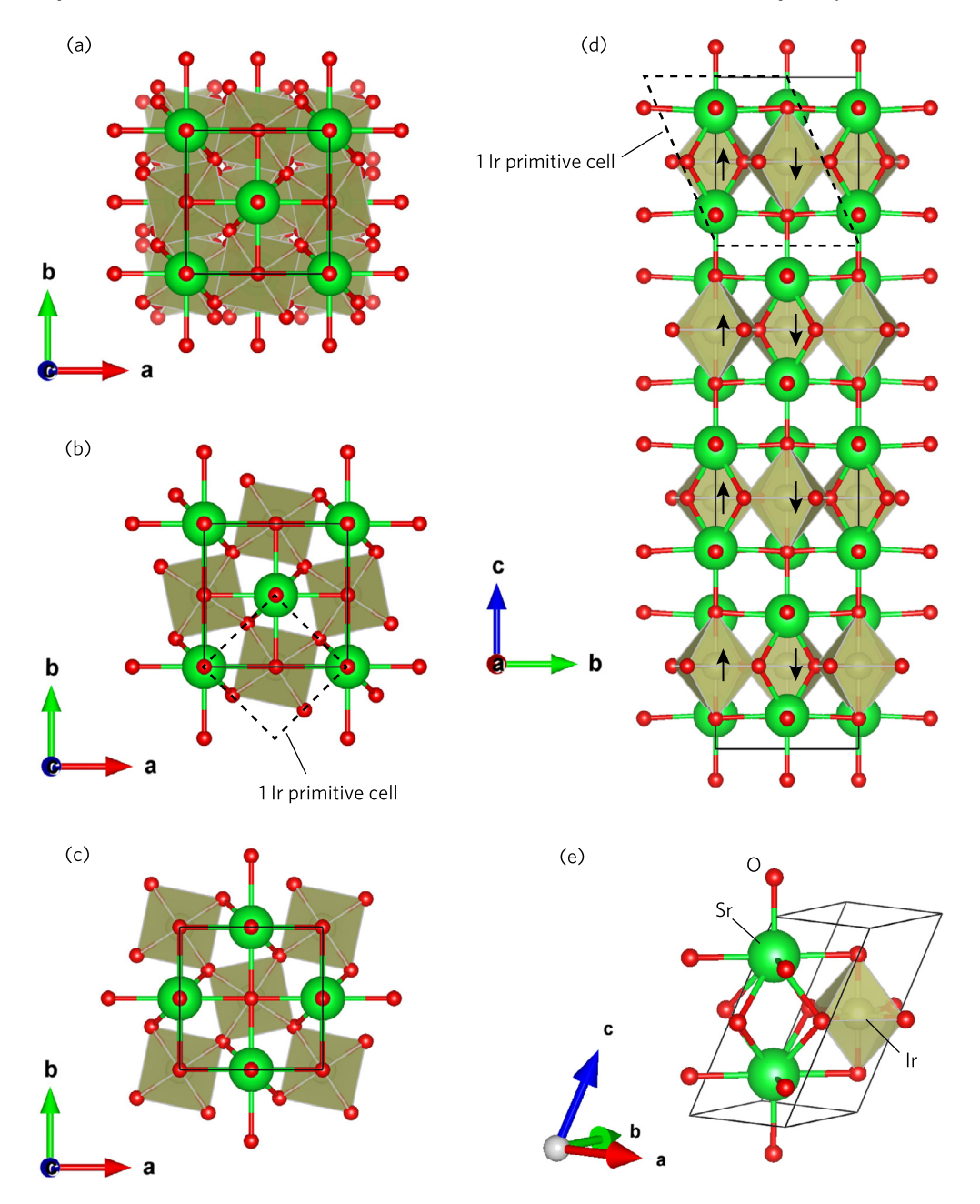


Fig. 2. Structure of Sr_2IrO_4 (space group 88, $I4_1/a$ (non-magnetic) or 13, P2/c (magnetic)): (a) top view, (b) top view with the first Ir layer only, (c) top view with the second Ir layer only, (d) side view with arrows showing the magnetic ordering, and (e) primitive 1-Ir unit cell (space group 139, I4/mmm) obtained from the supercell without octehedral tilting using the transformation matrix of $P^{-1} = (1/2, 1/2, 1/2, 1/2, 1/2, 0; 0, 0, 1/4)$. The octahedral tilting is present on panels (a)–(d).

points for each section of the path, as well as the transformation matrix P as inputs.

\$ octave fold.m

The folding is achieved by the following matrix product [19]

$$\tilde{\mathbf{K}} = \tilde{\mathbf{k}} P \mod 1. \tag{17}$$

The generated unique $\tilde{\mathbf{K}}$ points are stored in the case.klist_band file in a WIEN2k native format as three integer numbers per k point with a common integer divisor. It is important to note conventions used within WIEN2k to interpret k point coordinates in the case.klist_band file. The BZ of a conventional lattice is implied for face-centered (F), body-centered (B), C-base-centered (CXY), A-base-centered (CYZ), and B-base-centered (CXZ) orthorhombic lattices. The BZ of a primitive lattice is used for other lattice types (primitive(P), hexagonal (H), rhombohedral (R), B-base-centered (CXZ) monoclinic). Those peculiarities affect the

selection of supercell lattice vectors A in Eq. (3) and the construction of P matrix using Eq. (4). In practice, we expect that majority of users will have P-type supercells due the symmetry broken by disorder/defects.

WIEN2k: Now we generate eigenvalues and eigenvectors (wave functions or vector files) for the list of k points in the case.klist_band file. We use files saved in the SOC folder after the previous SCF step.

\$ x lapw1 -band -up [-p]

\$ x lapw1 -band -dn [-p]

\$ x lapwso -up [-orb] [-p]

The -orb switch is activated for the DFT+U calculation. Here we produce files that are essential for unfolding: case.vectorso[up/dn] (wave functions and energy eigenvalues) and case.normso[up/dn] (spinor components α^2 and β^2).

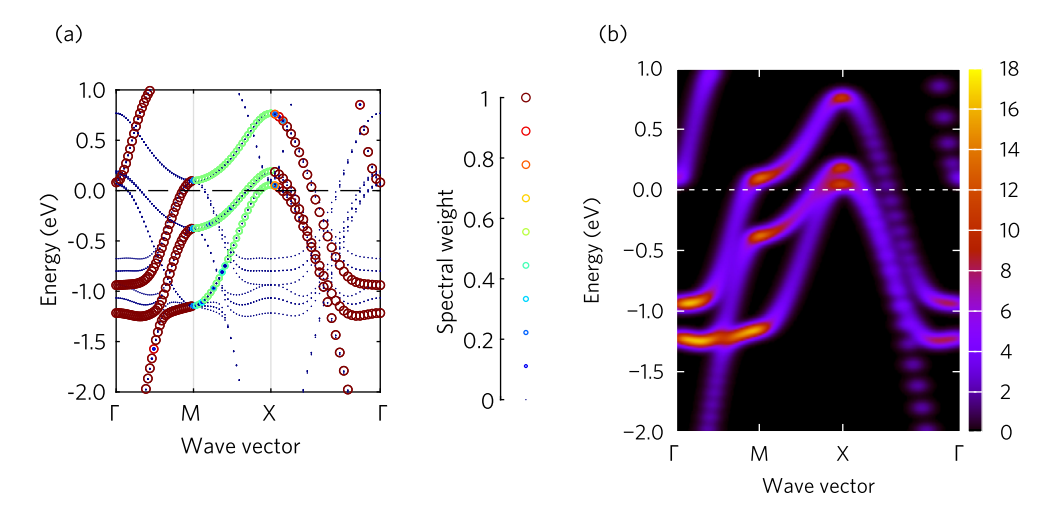


Fig. 3. Styles of presenting the unfolded band structure: (a) bubble plot of spectral weights $w_n(\mathbf{k})$ defined by Eq. (15), (b) spectral function A(E, k) defined by Eq. (18) in units of eV⁻¹ bohr calculated with Gaussian broadening parameters of $\sigma_E = 0.04$ eV and $\sigma_k = 0.006$ bohr⁻¹. Note that the hot spots on panel (b) are associated with areas of higher density of bubbles on panel (a) even though the bubbles have the same weight (e.g., the region of -1.5...-0.5 eV along the Γ-M segment).

VASP: Perform a non-SCF calculation (ICHARG=11 option in the INCAR file) using the charge density from SCF calculation (CHGCAR file). A suitable KPOINTS file generated by **fold.m** utility should be provided to substitute that used in the SCF calculation. The weight of k points in the KPOINTS file should be set to 1. The non-SCF calculation should store wave functions in the WAVECAR file (LWAVE=.TRUE. option in the INCAR file).

fold2Bloch: fold2Bloch is a FORTRAN code that can be compiled with either Intel or GNU FORTRAN compilers. In the case of WIEN2k, it takes wave functions, spinor components, and the transformation matrix P as input arguments

\$ fold2Bloch -so case.vectorsoup[_1] case. vectorsodn[1]

... case.normsoup[_1] case.normsodn[_1]
... "'P11 P12 P13:P21 P22 P23:P31 P32 P33'"

and generates a case.f2b file. If WIEN2k calculations run in a k-parallel mode ([-p] option), output vector and norm files will be marked with $_XX$ for each parallel stream. These files can be processed individually, and the output can be concatenated into one case.f2b file. The sample listing of the output file is given below

k_1	k_2	k_3	E (Ry)	W
0.000000	0.000000	0.000000	0.393800	0.001619
0.000000	0.000000	0.250000	0.393800	0.001019
0.000000	0.000000	0.500000	0.393800	0.487296
0.000000	0.000000	0.750000	0.393800	0.000001
0.500000	0.500000	0.000000	0.393800	0.000000
0.500000	0.500000	0.250000	0.393800	0.255542
0.500000	0.500000	0.500000	0.393800	0.000000
0.500000	0.500000	0.750000	0.393800	0.255542
0.000000	0.000000	0.000000	0.394518	0.374261
0.00000	0.000000	0.250000	0.394518	0.000001
0.000000	0.000000	0.500000	0.394518	0.001956
0.00000	0.000000	0.750000	0.394518	0.000001
0.500000	0.500000	0.000000	0.394518	0.000000
0.500000	0.500000	0.250000	0.394518	0.311889
0.500000	0.500000	0.500000	0.394518	0.000000
0.500000	0.500000	0.750000	0.394518	0.311893

Here one can see results of band unfolding with the transformation matrix $P = [1, \bar{1}, \bar{2}; 1, 1, \bar{2}; 0, 0, 4]$ and the volume scale of $n_{\rm V} = 8$. Two groups of eigenvalues are shown each unfolded into eight new k points (fractional coordinates) in the primitive BZ. Even though both eigenvalues belong to Γ point in the supercell BZ, after unfolding the first does not have any notable Γ character

(only ca. 0.16%), while the second eigenvalue retains about 37% of its Γ character.

In the case of VASP, fold2Bloch takes the wave function file and the transformation matrix *P* as mandatory input arguments \$ fold2Bloch WAVECAR "P11 P12 P13:P21 P22 P23: P31 P32 P33" [-ncl]

The optional argument '-ncl' should be included if the WAVE-CAR file was generated by the non-collinear vasp_ncl executable (e.g., necessary with SOC). The output is written in WAVE-CAR_spin1.f2b file for non-magnetic calculations (ISPIN=1 option in the INCAR file), or WAVECAR_spin1/2.f2b files for magnetic calculations (ISPIN=2 option in the INCAR file), or WAVECAR_spinor.f2b when the wave function is a spinor. The output file format is the same as the listing above, except the eV units are used for energy.

Utils/ubs_dots.m: This MATLAB script generates a plot of the unfolded band structure using a 'bubble' style as shown in Fig. 3a. The inputs are the case.f2b file, the desired \tilde{k} path in the primitive BZ (it has to match that used as input in fold.m), reciprocal lattice vectors of the supercell (can be read from the WIEN2k case.outputkgen file in a column-wise manner and later transposed within the script or from the VASP OUTCAR file), the Fermi energy from the WIEN2k case.scf file or the VASP OUTCAR. It is advised to exclude data points with a very low Bloch spectral weight (typically w < 0.05 via a threshold-weight input parameter) not to obscure the plot. The script generates a publication-quality plot (case.eps). This method is recommended for faster preview. The downside of this plot style is that the weights are not additive for degenerate data points (with the same energy and the wave vector). For instance, in Fig. 3a the M-X section visually appears with the Bloch weight of 0.5, which is different from $\Gamma - M$ and $X - \Gamma$ sections where the weight is 1. In fact, there is no difference in the total weight between sections since each data point along the M-X section splits into two degenerate points with the weight of 0.5 each. This issue is addressed in a 'spectral function' plotting style presented below. It is also possible to use IGOR plotting software for a scatter plotting style (a detailed workflow can be found in Zenodo repository [33]).

Utils/ubs_bmp.m: This Octave script is used to prepare a binary file case.f2b.bin for band structure plotting as a spectral function. The script uses same input as $ubs_dots.m$ with addition of smearing parameters for a Gaussian function in energy and k space and no filter for low weight points.

\$ octave ubs_bmp.m

The unfolded band structure is represented by a spectral function $A(E, \mathbf{k})$ constructed based on the output of discrete energy eigenvalues, unfolded $\tilde{\mathbf{k}}$ points, and associated Bloch spectral weights $w_n(\tilde{\mathbf{k}})$

$$A(E, \mathbf{k}) = \sum_{n \ k'} f(E - E_n, \sigma_E) f(|\mathbf{k} - \mathbf{k}'|, \sigma_k) w_n(k')$$
(18)

using a Gaussian smearing function

$$f(x,\sigma) = \sigma^{-1}(2\pi)^{-1/2} \exp\left[-x^2/(2\sigma^2)\right].$$
 (19)

This spectral function has an artificial broadening introduced to aid with the visual representation of single-particle eigenvalues and should not be confused with a spectral function used in manybody physics of interacting systems [34]. Sensible values for the energy and k space smearing are about 1/50 of the energy range and the k path length selected for the band structure plot. At the end of execution, XTICKS and KLABEL vectors are printed. They need to be noted and used in the next stage.

Utils/f2b-band-structure.plt: Finally, the unfolded band structure is plotted using Gnuplot with the input binary file case.f2b.bin.

\$ gnuplot f2b-band-structure.plt

The Gnuplot script incorporates data from XTICKS and KLABEL vectors used for labeling the high-symmetry points along the path and generates a publication-quality plot (case.eps). A sample of the spectral function plot is shown in Fig. 3b. We can see that the issue of a lower spectral weight for the M-X section is now resolved, and this section does not look suddenly different from $\Gamma-M$ and $X-\Gamma$ sections as in Fig. 3a. However, the downside is a new interpretation of the color bar, which is in units of eV⁻¹ bohr for the spectral function in contrast to Bloch spectral weights being always in the range $0\dots 1$. It will be more difficult to compare the scale between plots generated using different smearing parameters or different k point density along the path.

A workflow diagram that illustrates above steps is presented in Fig. 4.

2.5. Experimental details

The experimental structure of $\mathrm{Sr_2IrO_4}$ was measured with ARPES on the Cassiopée beamline of the SOLEIL synchrotron, with a SCIENTA R-4000 analyzer and an overall resolution better than 15 meV. The temperature was 20 K, the photon energy was set to 100 eV and linear polarization in the plane containing $\Gamma-M$ was used. The samples were prepared using a self-flux method, as reported before [35,36].

We have grown SrIrO₃ thin films on SrTiO₃ (001) substrate using pulsed laser deposition. A frequency-tripled Nd:YAG laser ($\lambda = 355$ nm, f = 2.5 Hz, pulse duration 15 ns) was focused on a polycrystalline SrIrO3 target made by solid state synthesis. The substrate surface was prepared following the process described in Ref. [37] to obtain a uniform TiO₂ surface termination. The deposition was performed with the substrate heated at T = 600 °C and with oxygen partial pressure $P = 2.5 \times 10^{-1}$ mbar and monitored by in-situ reflection high-energy electron diffraction. The thin films were then cooled down to room temperature with the same oxygen partial pressure to compensate for any oxygen vacancy. Finally, we fully structurally and physically characterized our thin films by X-ray diffraction and reflectivity using a Brüker D8 advance diffractometer and by surface diffraction on SIXS beamline at SOLEIL synchrotron, atomic force microscopy and electronic transport, concluding to similar characteristics and properties to previous reports in the literature [38-40].

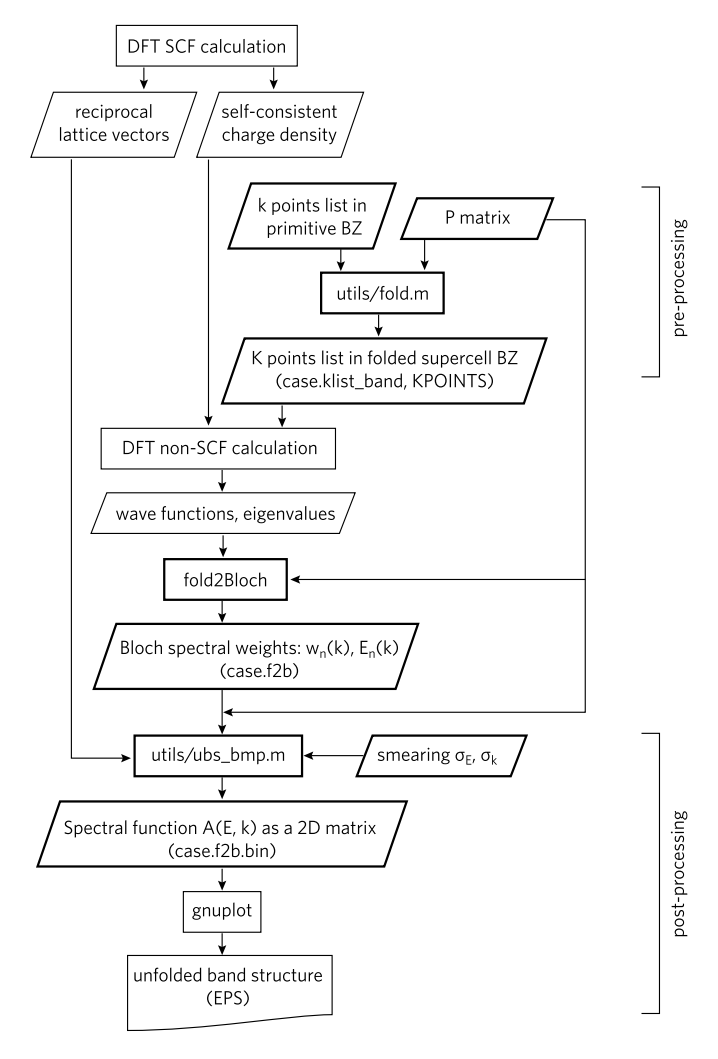


Fig. 4. Workrflow diagram for band structure unfolding with WIEN2k or VASP. Bold boundaries mark processes and data handled by fold2Bloch or its utilities.

3. Results and discussion

3.1. Sr₂IrO₄: theoretical calculations

The structure of $\rm Sr_2IrO_4$ was imported from Springer Materials [41] (dataset ID sd_1945591). The original structure is bodycentered tetragonal (BCT) and includes a tilting of $\rm IrO_6$ octahedra (Fig. 2a-d). The magnetic ordering further reduces the symmetry to a tetragonal cell with 8-Ir atoms. Its lattice vectors matrix (Å) is

$$A = \begin{bmatrix} 5.485 & 0 & 0 \\ 0 & 5.485 & 0 \\ 0 & 0 & 25.775 \end{bmatrix}. \tag{20}$$

For verification purposes we also created an idealized structure by eliminating the octahedral tilting and magnetic ordering. Its elementary structural unit (a 1-Ir primitive BCT unit cell) is shown in Fig. 2e. The corresponding matrix of primitive lattice vectors is

$$a = \begin{bmatrix} A_1/2 & -A_2/2 & 0 \\ A_1/2 & A_2/2 & 0 \\ A_1/2 & 0 & A_3/4 \end{bmatrix}$$
 (21)

with A_1 , A_2 , A_3 being the length of supercell lattice vectors. Following Eq. (4) we obtain the transformation matrix

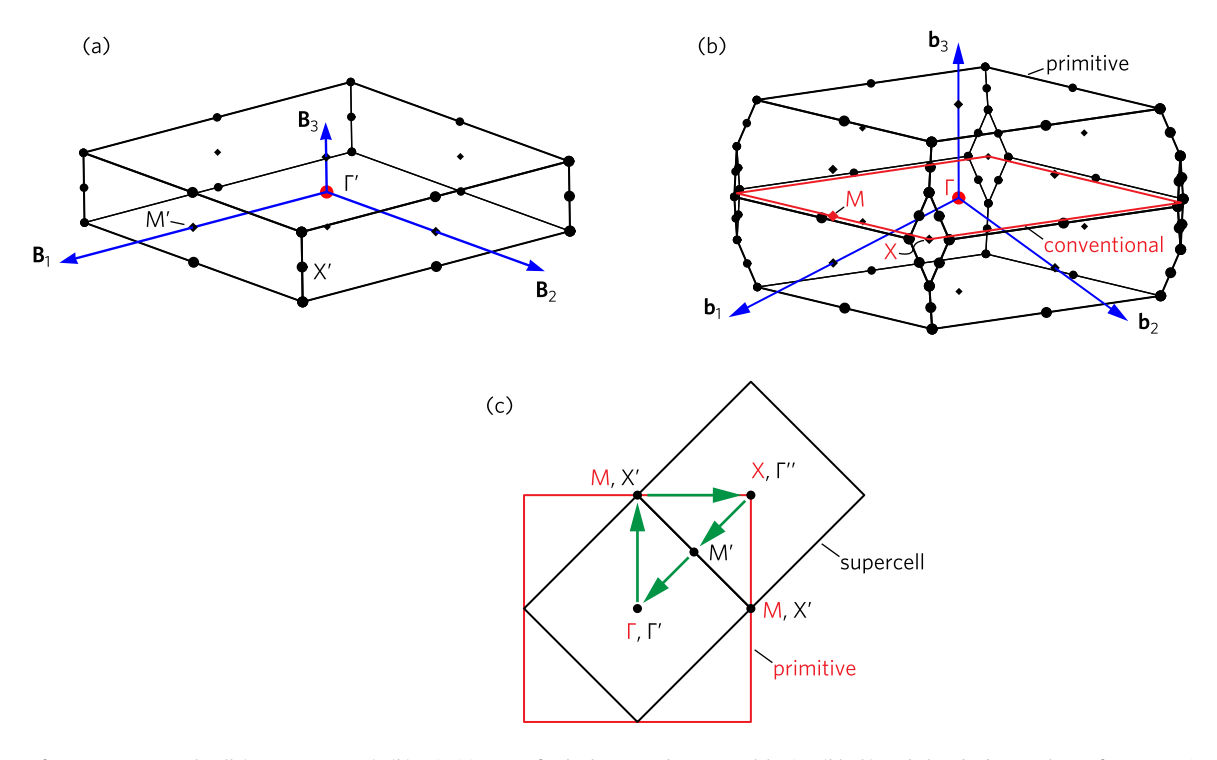


Fig. 5. (a) BZ of Sr_2IrO_4 tetragonal cell (space group 88). (b) Primitive BZ of a body-centred tetragonal lattice (black) and the $(k_x, k_y, 0)$ plane of a conventional BZ (red). (c) Overlay of the primitive and supercell BZ (top view). The k path of interest within the $(k_x, k_y, 0)$ plane is shown by green arrows.

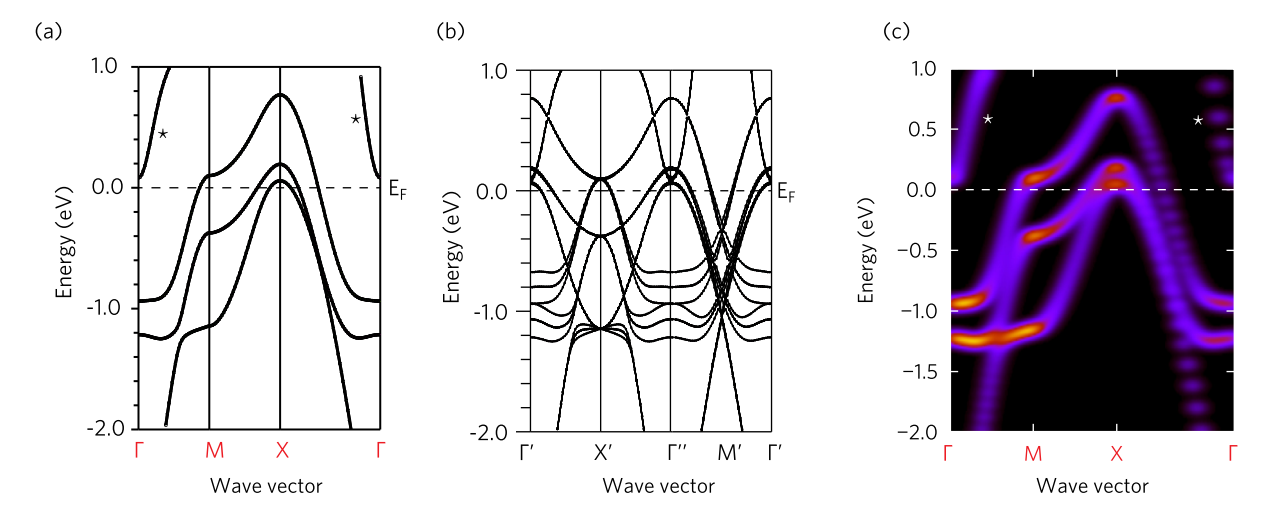


Fig. 6. Band structure of Sr_2IrO_4 at PBE+SOC level of theory without octehedral tilting: (a) body-centred tetragonal primitive cell (space group 139, 1-Ir atom), (b) tetragonal supercell (space group 88, 8-Ir atoms), (c) supercell unfolded into the primitive cell using $P = [1, \bar{1}, \bar{2}; 1, 1, \bar{2}; 0, 0, 4]$. The colorbar upper scale is 18 eV⁻¹ bohr. The asterisk (*) marks $d_{x^2-y^2}$ states. Energies are plotted relative to the Fermi energy. Red (black) labels for high-symmetry points in the reciprocal space refer to the primitive cell (supercell) BZ.

$$P = \begin{bmatrix} 1 & -1 & -2 \\ 1 & 1 & -2 \\ 0 & 0 & 4 \end{bmatrix},\tag{22}$$

which establishes the relation between 1-Ir primitive cell and 8-Ir supercell (without distortions). It should be noted that our selection of 1-Ir BCT primitive lattice vectors in Fig. 2e is not standard. This choice is motivated by the visual appearance of the primitive cell in relation to the supercell showing the 45° rotation and $2^{-1/2}$ scaling in the basal plane combined with tilting of the vertical \mathbf{a}_3 axis. This choice is not required, and identical results would be obtained with a standard choice. The structure files (in a WIEN2k native format) are available externally at Zenodo file repository [33] and can be visualized with XcrySDen [42] or VESTA [20].

The BZ of 8-Ir and 1-Ir cell is shown in Fig. 5a,b, respectively. For plotting band structures we selected the $\Gamma-M-X-\Gamma$ path. Since we made a non-standard choice for BCT primitive lattice vectors (see Table 9.1.7.2, tI Bravais lattice in the International tables for crystallography [43]), special care should be taken to map k point coordinates from the conventional to the primitive cell (Fig. 5b) to ensure that the coordinates are compatible with the chosen definition for lattice vectors (Table 2).

For verification purposes we first need to calculate the band structure *without* tilting of IrO_6 octehedra. This way we can establish a direct comparison between the 8-Ir cell and the primitive 1-Ir BCT cell. It is convenient to do this comparison at the PBE level of theory, since it leads to a non-magnetic solution with a more simple band structure (Fig. 6a). Bands near the Fermi energy are due to Ir-d electrons: the dispersive bands starting off Γ near

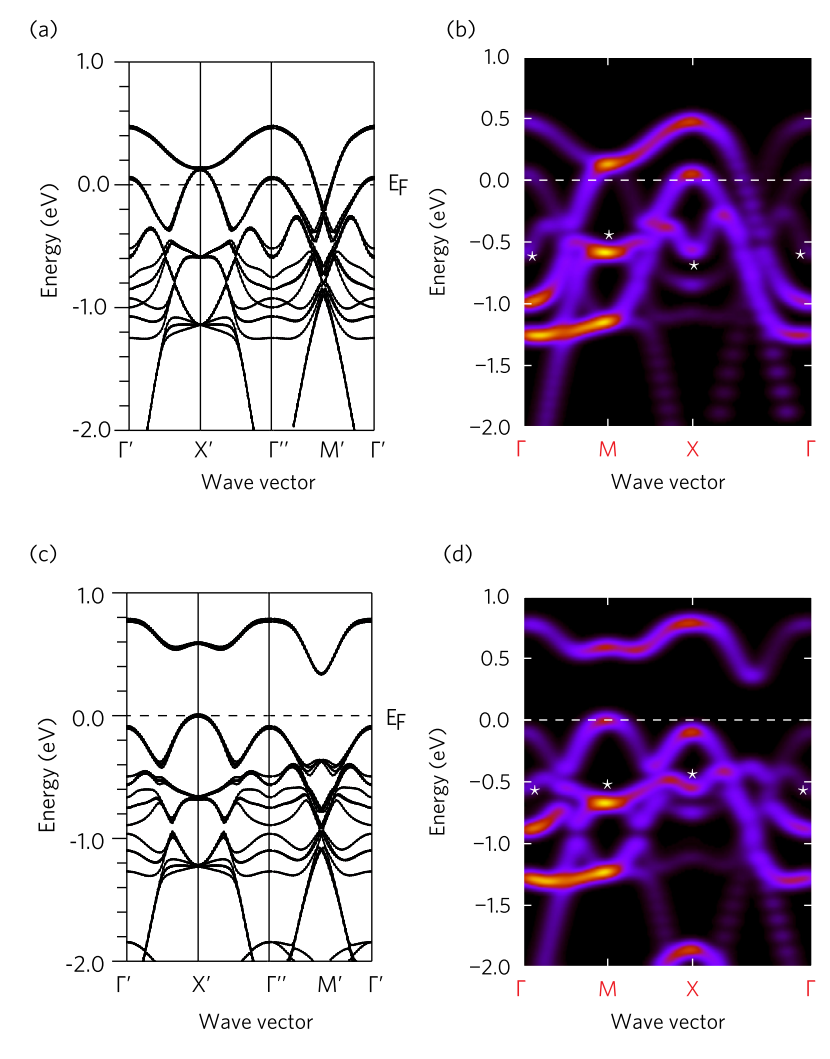


Fig. 7. Band structure of Sr_2IrO_4 with octehedral tilting: (a,b) PBE+SOC folded and unfolded, (c,d) PBE+SOC with onsite $U_{\rm eff}=3$ eV for Ir-d. Energies are plotted relative to the Fermi energy. The asterisk (*) marks d_{xy} states. The colorbar upper scale is 16 eV⁻¹ bohr for both panels.

Table 2 BCT reciprocal lattice points.

Label	Conventional [21]	Primitive (standard [21])	Primitive (Fig. 5c)
Γ	(0, 0, 0)	(0, 0, 0)	(0, 0, 0)
X	(1/2, 1/2, 0)	(0, 0, 1/2)	(1/2, 1/2, 1/2)
M	(1/2, 0, 0)	(-1/4, 1/4, 1/4)	(1/2, 0, 1/4)

 $E_{\rm F}$ correspond to the $d_{x^2-y^2}$ orbital; the remaining bands are due to t_{2g} states (d_{xy} , d_{yz} , and d_{xz} orbitals); the d_{z^2} orbital belongs to e_g states located at higher energies outside the energy range of interest

Fig. 6b shows the band structure of the 8-Ir supercell without octahedral tilting. This band structure is obscured by the zone folding. Fig. 5c can help to rationalize zone folding at high-symmetry k points (prime indices are for the supercell). Eigenvalues at both Γ and X points are folded into Γ' of the supercell. Eigenvalues at M point fall into X'. The band crossings along the $\Gamma'-X'$ segment are folding artefacts not observed in the primitive cell. The unfolded and primitive band structures are identical (Fig. 6a,c) that gives confidence in our approach and its implementation.

The realistic structure of $\rm Sr_2IrO_4$ includes tilting of $\rm IrO_6$ octahedra. Those distortions cause perturbations in the band structure, which can be assessed thanks to the new functionality of fold2Bloch. The unfolded band structure of 8-Ir cell with oc-

tahedral rotations (Fig. 7b) can now be compared to Fig. 6c (both calculated at the PBE level of theory). The most notable change is that the rotation allows hybridization between $d_{x^2-y^2}$ and d_{xy} , as is also the case in $\mathrm{Sr_2RhO_4}$ [44]. Therefore, new $d_{x^2-y^2}$ states move to higher energies (not visible in Fig. 7) and d_{xy} states are now pushed below the Fermi energy resulting in a new bright 'spot' at X below the Fermi energy (Fig. 7b), which is unfolded from Γ'' leaving a weak replica at Γ . Interestingly, states at M point are immune to the distortions due to octahedral rotations, because the 4-fold screw symmetry maintains degenerate doublets between the original t_{2g} bands and the folded bands (see Supporting information for additional insight).

To account for correlation effects we added the Hubbard $U_{\rm eff}=3$ eV correction for Ir-d states. The magnitude of $U_{\rm eff}$ was chosen to reproduce the experimental band gap of 0.5 eV [45,46]. Unlike PBE, PBE+U favors a magnetic solution with the moment of $\mu({\rm Ir})\approx 0.24\mu_{\rm B}$ per Ir site (the ordering is shown in Fig. 2d with the [001] spin quantization direction for simplicity). Experimental $\mu({\rm Ir})$ moments are 0.21 [30], 0.29 [47], and 0.37 [48]. A gap opens up between the on-site spin up and down states, which is particularly clear at M and at the middle of $\Gamma-X$ (Fig. 7c-d).

3.2. Sr_2IrO_4 : comparison with experiment

Fig. 8(a) shows the ARPES spectral intensity along the k-path $\Gamma - M - X - \Gamma$, which was extracted from our measurement using a

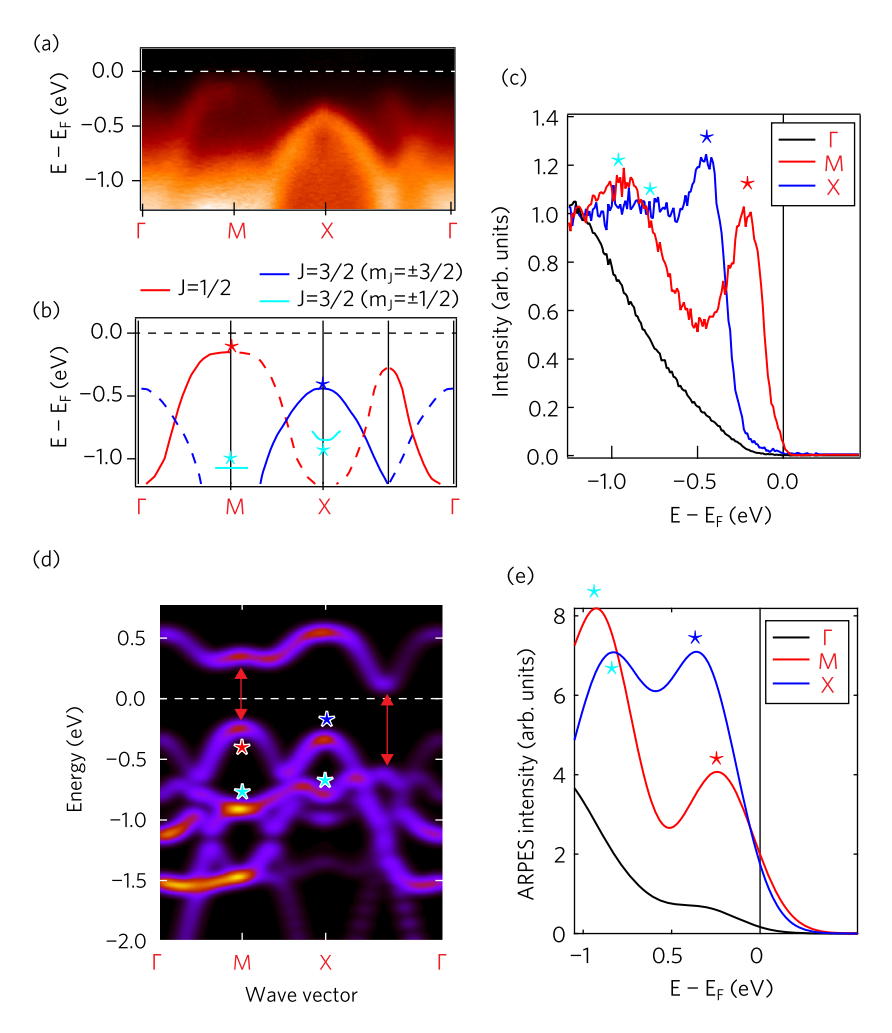


Fig. 8. (a) Energy-momentum plot of the ARPES intensity as a function of the path $\Gamma - M - X - \Gamma$. (b) Sketch of the dispersion of the main bands visible in ARPES. The lines are guides to the eyes extracted from the data, the colors are given by comparison to the calculation. (c) Energy distribution curves at X (blue), Γ (black) and M (red). (d) Comparison with the unfolded calculation along the same path. The red arrow mark the opening of the magnetic gap. The colorbar upper scale is 16 eV⁻¹ bohr. (e) Calculated ARPES spectra at X, Γ , and M (see text for details). Position of the Fermi energy in calculations was adjusted to match the experimental energy distance between the Fermi energy and the J=1/2 band maximum at M (red star) on the panel (c).

photon energy of 100 eV and a linear polarization along $\Gamma-M$ [35]. The different bands observed in this plot are sketched in Fig. 8(b) by red and blue guides to the eyes, the color corresponds to their dominant orbital character, characterized by the effective value of the total electronic angular momentum J, either J=1/2 ($m_J=\pm 1/2$) or J=3/2 ($m_J=\pm 1/2,\pm 3/2$). These data are similar to several previous reports [36,49,50], where more details can also be found.

The most intense band is the I = 3/2 band at X (blue star). Although it should also be present at Γ , which is equivalent in the supercell (see Fig. 5(c)), it can hardly be distinguished there. This is perfectly captured by the unfolded calculation of Fig. 8(d), which features much lower intensity for this band at Γ compared to X. A comparison of the measured and calculated intensity along Γ and X is also shown in Fig. 8(c) and (e), respectively. ARPES spectra in Fig. 8(e) were calculated based on the discrete spectral weights $w_n(\mathbf{k})$ defined by Eq. (15) and energies $E_n(\mathbf{k})$ of the unfolded band structure at specific k points. A Gaussian broadening of the width $\sigma = 0.2$ eV was applied. However, it is still a very crude approximation as other relevant details were omitted (matrix elements for initial- and final-state crystal wave functions, finite-lifetime effects, surface discontinuity, multiple scattering [51]). These matrix elements will further modulate the measured intensity, but the qualitative difference is well captured by the calculation. However, the relative position of the I = 3/2 band at X and I = 1/2 band at M is quite different in the two cases. In experiment, those bands are ca. 0.22 eV apart, while in calculations the energy difference between the valence band maxima at M and X is ca. 0.11 eV (compare red and blue stars on Fig. 8 panels (c) and (e)). This discrepancy is due to an underestimation of the effective spin-orbit coupling already noticed and discussed in the literature [52,53].

The J=1/2 band is the one where the magnetic gap opens [50] (Fig. 8(d), red arrows). This band is clearly visible along $\Gamma-M$, but much weaker along M-X, two paths expected to be equivalent in the supercell. Again, this fits with the theoretical calculation. Similarly, the J=1/2 band drastically loses weight on the second half of $\Gamma-X$, both in the experiment and in calculation. Note that, as the relative positions of J=1/2 and J=3/2 are not correctly captured, the break in the dispersion due to hybridization between J=1/2 and J=3/2 where they cross is also shifted.

The other bands are more difficult to isolate in ARPES, either because they become too broad at high binding energies or because they have low intensity in these experimental conditions. However, it is clear that another band is present at -0.8 eV at M and a trace of a second band at X can be seen. They are marked by cyan stars and correspond well to the other J=3/2 band ($m_J=\pm 1/2$), which is dominated by d_{xy} weight, and therefore has a lower cross section in ARPES [36].

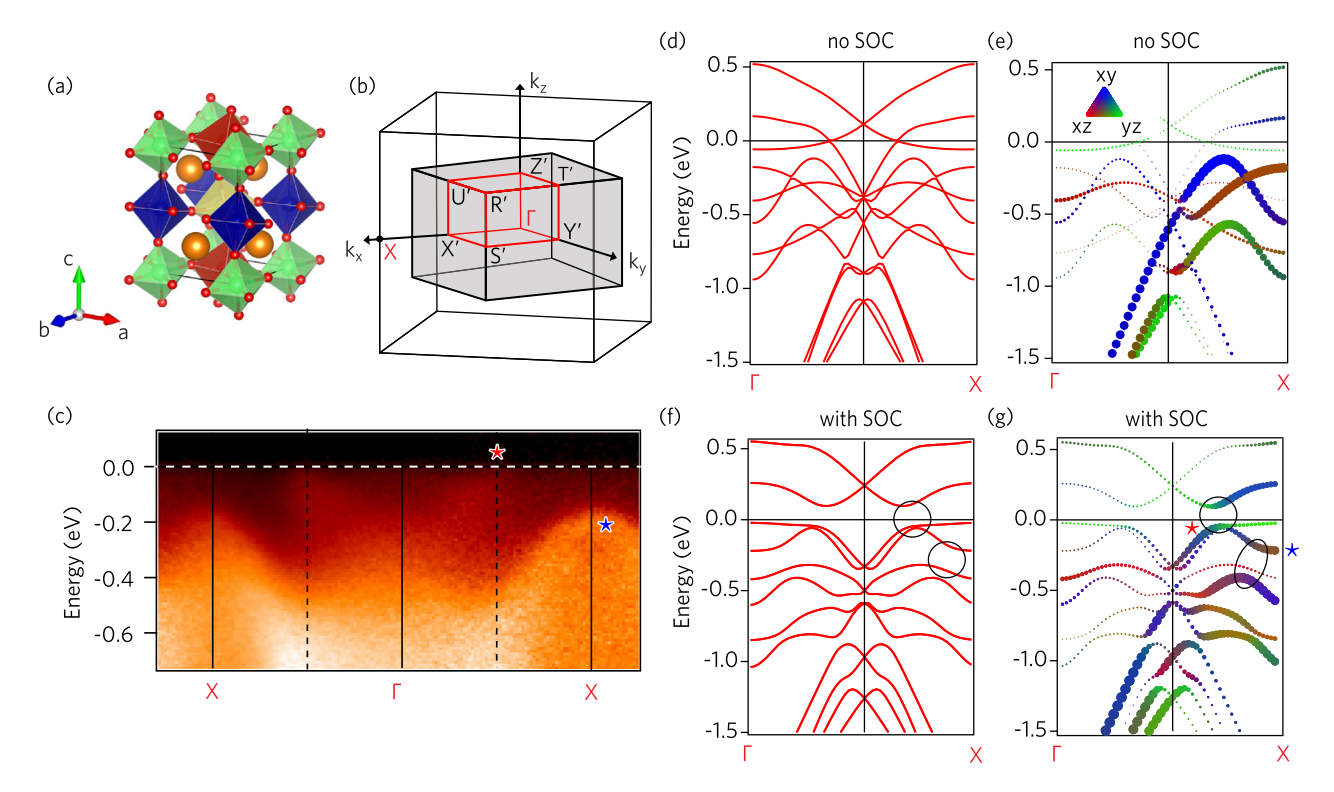


Fig. 9. (a) Sketch of the SrIrO₃ structure. There are 4 inequivalent Ir, at the center of oxygen octahedra of a different color. (b) Sketch of the corresponding BZ. The black cube corresponds to the primitive BZ (pseudocubic unit cell) and the shaded region to the supercell BZ. (c) Energy-momentum image of the dispersion along $\Gamma - X$ for a thin film of SrIrO₃/SrTiO₃, measured with 100 eV photon energy. The $\Gamma - X$ path is the diagonal of the primitive unit cell similar to Fig. 5(c). (d) Calculated band structure along $\Gamma - X$ for $k_z = 0$ without SOC. (e) Same as (d) with unfolding weight as marker size and color scale indicating d_{xz} (red), d_{yz} (green) and d_{xy} (blue) character. (f,g) Same as (d,e) with SOC. The circles highlight the regions where a large SOC-induced gap opens. The stars highlight bands discussed in the paper.

3.3. SrIrO₃: perspective

We illustrated the unfolding process with the case of $\rm Sr_2 IrO_4$, where the connection to a primitive unit cell, without rotation of the oxygen octahedra, is relatively easy to anticipate. However, in more complicated cases, it can become totally impossible to understand the band structure and compare it to ARPES data, without the help of the unfolding calculation.

A very interesting case is the related 3D iridate SrIrO₃. Its structure is shown in Fig. 9(a). In addition to in-plane rotation of the oxygen octahedra, similar to Sr₂IrO₄, it also exhibits a tilt of the oxygen octahedra from the c axis, inducing another type of folding along k_z . The resulting BZ is shown in Fig. 9(b), it is rotated 45° in the $(k_x, k_y, 0)$ plane, as for Sr_2IrO_4 , but also halved along k_z . The calculated band structure is semimetallic and the four J = 1/2folded bands are expected to form a Dirac nodal line around the U point (1/2, 0, 1/2) [54]. As topological features are rare in correlated oxides, this occurrence generated great interest. However, the orthorhombic structure of SrIrO₃ is only stable in thin films, which adds questions on the role of the epitaxial constraint and the survival of topological features in real systems [55]. It would therefore be very interesting to look for these features directly with ARPES, but the situation is not yet concluding. The only ARPES studies available to date were performed at a fixed photon energy [56,57], which may not allow one to precisely locate the U point, or at high photon energies, where the energy resolution is lower [58].

We only sketch here the help of unfolded calculations for deciphering the electronic structure of $SrIrO_3$, more details will be published later. Fig. 9(c) shows the images of the dispersion along $\Gamma - X$ direction with a photon energy of 100 eV obtained on a $SrIrO_3(001)$ thin film (t = 10.4 nm) grown on $SrTiO_3(001)$ substrates (for clarity, we keep the same labeling as previously for the ($k_X, k_Y, 0$) plane of Sr_2IrO_4 in Fig. 5(c), i.e., X labels the corner of the primitive 2D BZ similar to Fig. 5). The ARPES image

looks quite simple, with a prominent band at X (almost invisible at Γ), resembling the J=3/2 in $\mathrm{Sr_2IrO_4}$ shifted up by 0.2 eV and a band reaching the Fermi level at the middle of $\Gamma-X$, looking like J=1/2 in $\mathrm{Sr_2IrO_4}$ shifted up by 0.15 eV. Quantitatively, the comparison with raw calculations in the supercell is usually very confusing, as a much more complicated band structure is predicted [Fig. 9(f)]. We will show how unfolding of the band structure can simplify the picture.

We calculated with WIEN2k the electronic structure for the structure given in Table III of Ref. [59]. The space group is Pbnm (#62), and the parameters are given in Table III. As for Sr_2IrO_4 , we can define the lattice vector matrix of the supercell (Å) and the fictitious primitive cell, as well as the transformation matrix:

$$A = \begin{bmatrix} 5.597 & 0 & 0 \\ 0 & 5.568 & 0 \\ 0 & 0 & 7.892 \end{bmatrix},$$

$$a = \begin{bmatrix} A_1/2 & -A_2/2 & 0 \\ A_1/2 & A_2/2 & 0 \\ 0 & 0 & A_3/2 \end{bmatrix},$$

$$P = \begin{bmatrix} 1 & -1 & 0 \\ 1 & 1 & 0 \\ 0 & 0 & 2 \end{bmatrix}$$
(23)

No Coulomb repulsion U was used and a semi-metallic non-magnetic state is obtained by employing a non-spin-polarized calculation. This compound is paramagnetic in experiment [60].

Assuming our ARPES data at this photon energy correspond to $k_z = 0$, we show the calculated electronic structure in Fig. 9(d,f) with and without SOC. Clearly, the calculation looks much more complicated than ARPES data, and it is extremely difficult to understand which bands should be compared to the experiment.

After unfolding [Fig. 9(e,g)], a set of 3 bands is clearly emphasized, although their dispersions are affected by their mutual interactions. Using a color code for orbital characters (the case.ing file was modified to rotate a and b by 45° and align them with Ir-O-Ir bonds), one can clearly recognize the original $d_{xz}/d_{yz}/d_{xy}$ bands [panel (e), without SOC] and J = 1/2, J = 3/2 after their interaction with SOC [panel (g)]. The places where a SOC induced hybridization gap openings are noted as empty circles. Obviously the band marked by a red star is at significantly different position in the measurement, compared to the calculation. On the other hand, the band at X (blue star) exhibits a well-defined parabolic shape in the measurement over 0.4 eV, while there is a large SOC induced gap near the top of the dispersion in the calculation. Similar to Sr₂IrO₄, we can anticipate that the effective spin-orbit coupling may be underestimated in the calculation, which will change the splitting of the two bands and also the position of their crossing, hence the break in the dispersion. Moreover, as the shape of d_{xy} depends sensitively on the rotations, it may be necessary to tune the structure to get the right interaction pattern. This has extremely important consequences for the formation of the Dirac nodal line at $k_z = 1/2$, which we will not discuss here. These examples show how adjusting the structure to get a better description of the experimental data will be possible only when a basic understanding of the origin of the different bands is reached, thanks to the unfolding scheme.

Let us stress that the intensity of the folded bands is also a fine marker of the strength of the interactions at the origin of the supercell, which, in this case, is the rotations of the oxygen octahedra. In a similar spirit, the information contained in the intensity of the folded bands on these interactions was recently used to refine the structure of ${\rm SrRuO_3}$ thin films [61]. The near absence of the folded bands in our measurement suggests a small coupling. From the topological point of view, the meaning of the crossing of two bands with very different spectral weight is also a question that may deserve further work.

4. Conclusion

Unfolding of a supercell band structure into a primitive Brillouin zone is important for understanding implications of structural distortions, disorder, defects, and solid solutions on materials electronic structure. Necessity of the band unfolding is also recognized in interpretation of angle-resolved photoemission spectroscopy (ARPES) measurements. We described an extension of the fold2Bloch package by implementing an arbitrary transformation matrix used to establish a relation between primitive cell and supercell. The convention selected for the transformation matrix is compatible with that recommended by the International tables for crystallography. This development allows us to overcome limitations of supercells constructed exclusively by scaling of primitive cell lattice vectors. For instance, it becomes possible to transform between primitive and conventional cells as well as include rotations. The updated fold2Bloch package is available from a GitHub repository as a FORTRAN code. It interfaces with the all-electron full-potential WIEN2k and the pseudopotential VASP density functional theory packages. The fold2Bloch is supplemented by additional pre- and post-processing utilities that aid in generating k points in the supercell (such that they later fall onto a desired path in the primitive Brillouin zone after unfolding) and plotting the unfolded band structure. We selected Sr₂IrO₄ as an illustrative example and, for the first time, present its properly unfolded band structure in direct comparison with ARPES measurements. In addition, critical importance of the band unfolding for interpretation of SrIrO₃ ARPES data is illustrated and discussed as a perspective. Of particular interest for iridates is the ability of ARPES to sense imprints that tilting of IrO₆ octahedra leaves on the materials' electronic structure. ARPES measurements teach us an important lesson: small structural perturbations neither lead to a sudden change in the electronic structure nor redefine the associated primitive Brillouin zone, contrary to what is expected from the formal symmetry of the structure.

Declaration of competing interest

The authors declare the following financial interests/personal relationships which may be considered as potential competing interests:

Veronique Brouet reports financial support was provided by French National Research Agency. Calculations were performed using the Compute Canada infrastructure supported by the Canada Foundation for Innovation under John R. Evans Leaders Fund.

Data availability

The fold2Bloch source code is available from GitHub repositories for WIEN2k [31] and for VASP [32].

A ZIP archive with WIEN2k structures, relevant scripts, initialization and unfolding workflows required to reproduce these findings is available from Zenodo file repository [33]. See README file within the archive for additional description of the content.

Acknowledgements

Calculations were performed using the Compute Canada infrastructure supported by the Canada Foundation for Innovation under John R. Evans Leaders Fund. ARPES work was supported by the Agence Nationale de la Recherche grant "SOCRATE" (Grant No. ANR-15-CE30-0009-01).

Appendix A. Supplementary material

Supplementary material related to this article can be found online at https://doi.org/10.1016/j.cpc.2023.108800.

References

- [1] K. Niizeki, T. Akamatsu, J. Phys. Condens. Matter 2 (1990) 2759.
- [2] T. Kosugi, H. Nishi, Y. Kato, Y.-i. Matsushita, J. Phys. Soc. Jpn. 86 (2017) 124717.
- [3] S.G. Mayo, F. Yndurain, J.M. Soler, J. Phys. Condens. Matter 32 (2020) 205902.
- [4] T.G. Dargam, R.B. Capaz, B. Koiller, Phys. Rev. B 56 (1997) 9625.
- [5] T.B. Boykin, G. Klimeck, Phys. Rev. B 71 (2005) 115215.
- [6] T.B. Boykin, N. Kharche, G. Klimeck, M. Korkusinski, J. Phys. Condens. Matter 19 (2007) 036203.
- [7] L.-W. Wang, L. Bellaiche, S.-H. Wei, A. Zunger, Phys. Rev. Lett. 80 (1998) 4725.
- [8] V. Popescu, A. Zunger, Phys. Rev. Lett. 104 (2010) 236403.
- [9] V. Popescu, A. Zunger, Phys. Rev. B 85 (2012) 085201.
- [10] W. Ku, T. Berlijn, C.-C. Lee, Phys. Rev. Lett. 104 (2010) 216401.
- [11] P.V.C. Medeiros, S. Stafström, J. Björk, Phys. Rev. B 89 (2014) 041407.
- [12] P.V.C. Medeiros, S.S. Tsirkin, S. Stafström, J. Björk, Phys. Rev. B 91 (2015) 041116.
- [13] O. Rubel, A. Bokhanchuk, S.J. Ahmed, E. Assmann, Phys. Rev. B 90 (2014) 115202
- [14] V. Wang, N. Xu, J.-C. Liu, G. Tang, W.-T. Geng, Comput. Phys. Commun. 267 (2021) 108033.
- [15] Q. Zheng, PyVaspwfc, https://github.com/QijingZheng/VaspBandUnfolding, 2022.
- [16] B. Gruber, in: International Tables for Crystallography, 4th ed., Springer, 2006, pp. 756–760.
 [17] P.M. de Wolff, in: International Tables for Crystallography, 4th ed., Springer,
- 2006, pp. 750–755. [18] A.M. Glazer, Acta Crystallogr., Sect. B 28 (1972) 3384.
- [19] H. Arnold, in: International Tables for Crystallography, 4th ed., Springer, 2006, pp. 78–85.
- [20] K. Momma, F. Izumi, J. Appl. Crystallogr. 44 (2011) 1272.
- [21] M.I. Aroyo, D. Orobengoa, G. de la Flor, E.S. Tasci, J.M. Perez-Mato, H. Won-dratschek, Acta Crystallogr., Sect. A 70 (2014) 126.

- [22] P. Blaha, K. Schwarz, G.K.H. Madsen, D. Kvasnicka, J. Luitz, R. Laskowski, F. Tran, L.D. Marks, WIEN2k: An Augmented Plane Wave Plus Local Orbitals Program for Calculating Crystal Properties, Vienna University of Technology, Austria, 2018
- [23] P. Blaha, K. Schwarz, F. Tran, R. Laskowski, G.K.H. Madsen, L.D. Marks, J. Chem. Phys. 152 (2020) 074101.
- [24] G. Kresse, J. Furthmüller, Phys. Rev. B 54 (1996) 11169.
- [25] P.E. Blöchl, Phys. Rev. B 50 (1994) 17953.
- [26] G. Kresse, D. Joubert, Phys. Rev. B 59 (1999) 1758.
- [27] The FLEUR project, https://www.flapw.de/.
- [28] J.P. Perdew, K. Burke, M. Ernzerhof, Phys. Rev. Lett. 77 (1996) 3865.
- [29] V.I. Anisimov, I.V. Solovyev, M.A. Korotin, M.T. Czyżyk, G.A. Sawatzky, Phys. Rev. B 48 (1993) 16929.
- [30] F. Ye, S. Chi, B.C. Chakoumakos, J.A. Fernandez-Baca, T. Qi, G. Cao, Phys. Rev. B 87 (2013) 140406.
- [31] O. Rubel, A. Bokhanchuk, E. Assmann, fold2Bloch for WIEN2k (2022), https://github.com/rubel75/fold2Bloch-Wien2k.
- [32] O. Rubel, fold2Bloch for VASP, https://github.com/rubel75/fold2Bloch-VASP, 2022
- [33] O. Rubel, J.-B. Moussy, P. Foulquier, V. Brouet, Band unfolding with a general transformation matrix: from code implementation to interpretation of photoemission spectra (workflow), https://doi.org/10.5281/zenodo.7838856, 2023.
- [34] L. Reining, The GW approximation: content, successes and limitations, WIREs Comput. Mol. Sci. 8 (2017), https://doi.org/10.1002/wcms.1344.
- [35] V. Brouet, J. Mansart, L. Perfetti, C. Piovera, I. Vobornik, P.L. Fèvre, F. Bertran, S.C. Riggs, M.C. Shapiro, P. Giraldo-Gallo, I.R. Fisher, Phys. Rev. B 92 (2015) 081117.
- [36] A. Louat, B. Lenz, S. Biermann, C. Martins, F. Bertran, P.L. Fèvre, J.E. Rault, F. Bert, V. Brouet, Phys. Rev. B 100 (2019) 205135.
- [37] J.G. Connell, B.J. Isaac, G.B. Ekanayake, D.R. Strachan, S.S.A. Seo, Appl. Phys. Lett. 101 (2012) 251607.
- [38] S.G. Bhat, N. Gauquelin, N.K. Sebastian, A. Sil, A. Béché, J. Verbeeck, D. Samal, P.S.A. Kumar, Europhys. Lett. 122 (2018) 28003.
- [39] A. Gutiérrez-Llorente, L. Iglesias, B. Rodríguez-González, F. Rivadulla, APL Mater. 6 (2018) 091101.
- [40] L. Zhang, Q. Liang, Y. Xiong, B. Zhang, L. Gao, H. Li, Y.B. Chen, J. Zhou, S.-T. Zhang, Z.-B. Gu, S.-h. Yao, Z. Wang, Y. Lin, Y.-F. Chen, Phys. Rev. B 91 (2015) 035110.
- [41] F. Ye, X. Wang, C. Hoffmann, J. Wang, S. Chi, M. Matsuda, B.C. Chakoumakos, J.A. Fernandez-Baca, G. Cao, Phys. Rev. B 92 (2015) 201112.
- [42] A. Kokalj, Compos. Mater. Sci. 28 (2003) 155, code available from http://www.xcrysden.org/.

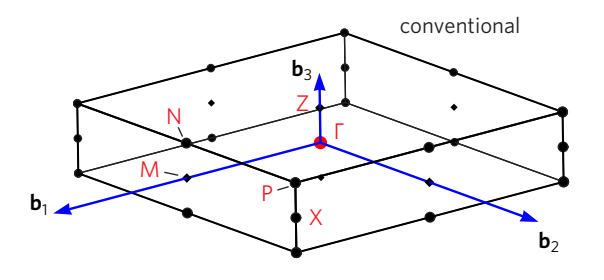
- [43] H. Burzlaff, H. Zimmermann, in: International Tables for Crystallography, 4th ed., Springer, 2006, pp. 742–749.
- [44] B.J. Kim, J. Yu, H. Koh, I. Nagai, S.I. Ikeda, S.-J. Oh, C. Kim, Phys. Rev. Lett. 97 (2006) 106401.
- [45] S.J. Moon, H. Jin, K.W. Kim, W.S. Choi, Y.S. Lee, J. Yu, G. Cao, A. Sumi, H. Funakubo, C. Bernhard, T.W. Noh, Phys. Rev. Lett. 101 (2008) 226402.
- [46] I. Battisti, K.M. Bastiaans, V. Fedoseev, A. de la Torre, N. Iliopoulos, A. Tamai, E.C. Hunter, R.S. Perry, J. Zaanen, F. Baumberger, M.P. Allan, Nat. Phys. 13 (2016) 21
- [47] S.W. Lovesey, D.D. Khalyavin, P. Manuel, L.C. Chapon, G. Cao, T.F. Qi, J. Phys. Condens. Matter 24 (2012) 496003.
- [48] C. Dhital, T. Hogan, Z. Yamani, C. de la Cruz, X. Chen, S. Khadka, Z. Ren, S.D. Wilson, Phys. Rev. B 87 (2013) 144405.
- [49] B.J. Kim, H. Jin, S.J. Moon, J.-Y. Kim, B.-G. Park, C.S. Leem, J. Yu, T.W. Noh, C. Kim, S.-J. Oh, J.-H. Park, V. Durairaj, G. Cao, E. Rotenberg, Phys. Rev. Lett. 101 (2008) 076402.
- [50] C. Martins, B. Lenz, L. Perfetti, V. Brouet, F. Bertran, S. Biermann, Phys. Rev. Mater. 2 (2018) 032001.
- [51] A. Damascelli, Z. Hussain, Z.-X. Shen, Rev. Mod. Phys. 75 (2003) 473.
- [52] G.-Q. Liu, V.N. Antonov, O. Jepsen, O.K. Andersen, Phys. Rev. Lett. 101 (2008) 026408.
- [53] S. Zhou, K. Jiang, H. Chen, Z. Wang, Phys. Rev. X 7 (2017) 041018.
- [54] J.-M. Carter, V.V. Shankar, M.A. Zeb, H.-Y. Kee, Phys. Rev. B 85 (2012) 115105.
- [55] J. Liu, D. Kriegner, L. Horak, D. Puggioni, C.R. Serrao, R. Chen, D. Yi, C. Frontera, V. Holy, A. Vishwanath, J.M. Rondinelli, X. Marti, R. Ramesh, Phys. Rev. B 93 (2016) 085118.
- [56] Y.F. Nie, P.D.C. King, C.H. Kim, M. Uchida, H.I. Wei, B.D. Faeth, J.P. Ruf, J.P.C. Ruff, L. Xie, X. Pan, C.J. Fennie, D.G. Schlom, K.M. Shen, Phys. Rev. Lett. 114 (2015) 016401
- [57] Z.T. Liu, M.Y. Li, Q.F. Li, J.S. Liu, W. Li, H.F. Yang, Q. Yao, C.C. Fan, X.G. Wan, Z. Wang, D.W. Shen, Sci. Rep. 6 (2016) 30309.
- [58] P. Schütz, D.D. Sante, L. Dudy, J. Gabel, M. Stübinger, M. Kamp, Y. Huang, M. Capone, M.-A. Husanu, V.N. Strocov, G. Sangiovanni, M. Sing, R. Claessen, Phys. Rev. Lett. 119 (2017) 256404.
- [59] D. Puggioni, J.M. Rondinelli, J. Appl. Phys. 103 (2008) 103706, J. Appl. Phys. 119 (2016) 086102.
- [60] J.G. Zhao, L.X. Yang, Y. Yu, F.Y. Li, R.C. Yu, Z. Fang, L.C. Chen, C.Q. Jin, J. Appl. Phys. 103 (2008) 103706.
- [61] B. Sohn, C. Kim, Evolution of electronic band reconstruction in thickness-controlled perovskite SrRuO₃ thin films, J. Korean Phys. Soc. (2022), https://doi.org/10.1007/s40042-022-00633-5.

SUPPLEMENTARY INFORMATION

Title: Band unfolding with a general transformation matrix: from code implementation to interpretation of photoemission spectra

Authors: Oleg Rubel, Jean-Baptiste Moussy, Paul Foulquier, and Véronique Brouet

The purpose of this section is to rationalize 'immunity' of Ir- $d t_{2q}$ states in Sr_2IrO_4 at M point to the distortions due to octahedral rotations. More specifically, there are no additional states or visible changes in degeneracy at M point of the distorted structure (Fig. 7b) as compared to the structure without octahedral rotations (Fig. 6c). The explanation relies on symmetry arguments combined with the zone folding. This result is a combination of several factors: (i) symmetry of the C_{2v} wave vector point group at M, (ii) symmetry of Ir layers in the tetragonal structure of $\mathrm{Sr_2IrO_4}$ with octahedral rotations, (iii) nearly absent dispersion of Ir-d t_{2g} states at M along the tetragonal c axis, and (iv) absence of other k points within the $(k_x, k_y, 0)$ plane that fold into M. Based on the WIEN2k irrep analysis program and the Bilbao crystallographic server (KVEC module [21]), the M point of the primitive cell belongs to C_{2v} point group. According to a character table of the C_{2v} point group, d_{xy} , d_{xz} , and d_{yz} states are associated with different irreducible representations. Thus, these states are already non-degenerate in the undisturbed structure (see Fig. 6a). The structure of Sr₂IrO₄ with octahedral rotations (Fig. 2, non-magnetic space group 88, I4₁/a) consist of four Ir layers. The layers are identical and connected via 4-fold screw symmetry operations implying that all Ir atoms have an identical chemical environment. We do not observe additional states folding into X' within the energy range of the plot in Fig. 6b. It is partly because the band dispersion of Ir-d t_{2g} states is rather 'flat' in direction perpendicular to the layers (see Fig. S1 k path section M-N), which precludes us from observing signs of band folding along the tetragonal c axis. Also, there are two equivalent M points, (1/2,0,0) and (0, 1/2, 0), in the tetragonal BZ, and both points correspond to X' in the supercell (Fig. 5c). Thus, there are no k points other than M folded into X' within the $(k_x, k_y, 0)$ plane of the primitive BZ (see the band structure of an isolated two-dimensional layer in Fig. S2 as an additional proof). These factors explain why Ir-d t_{2g} states at the M point are robust against octahedral rotations.



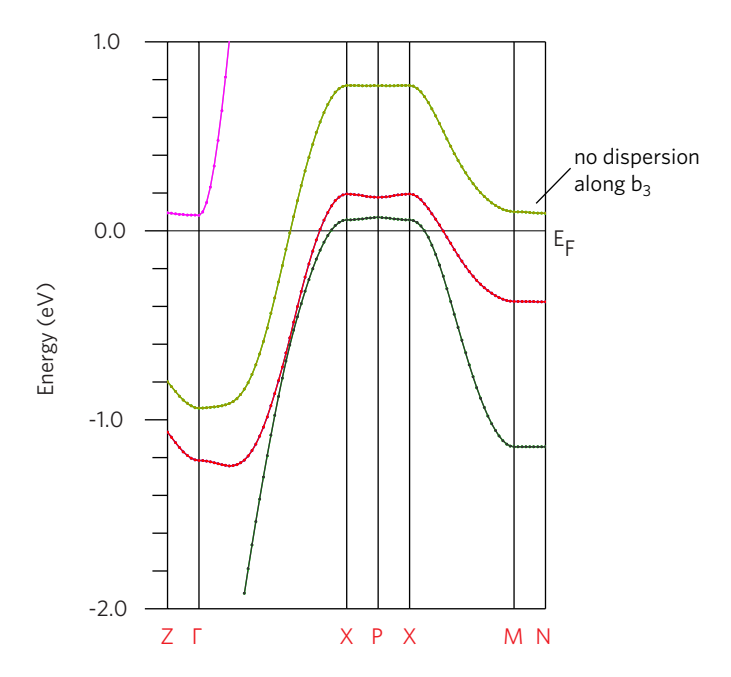


FIG. S1. Band structure of Sr_2IrO_4 body-centred tetragonal primitive cell (space group 139, 1-Ir atom, without octehedral tilting) at PBE+SOC level of theory. Ir-d t_{2g} states at M point show no dispersion along \mathbf{b}_3 reciprocal lattice vector, which corresponds to the tetragonal c axis.

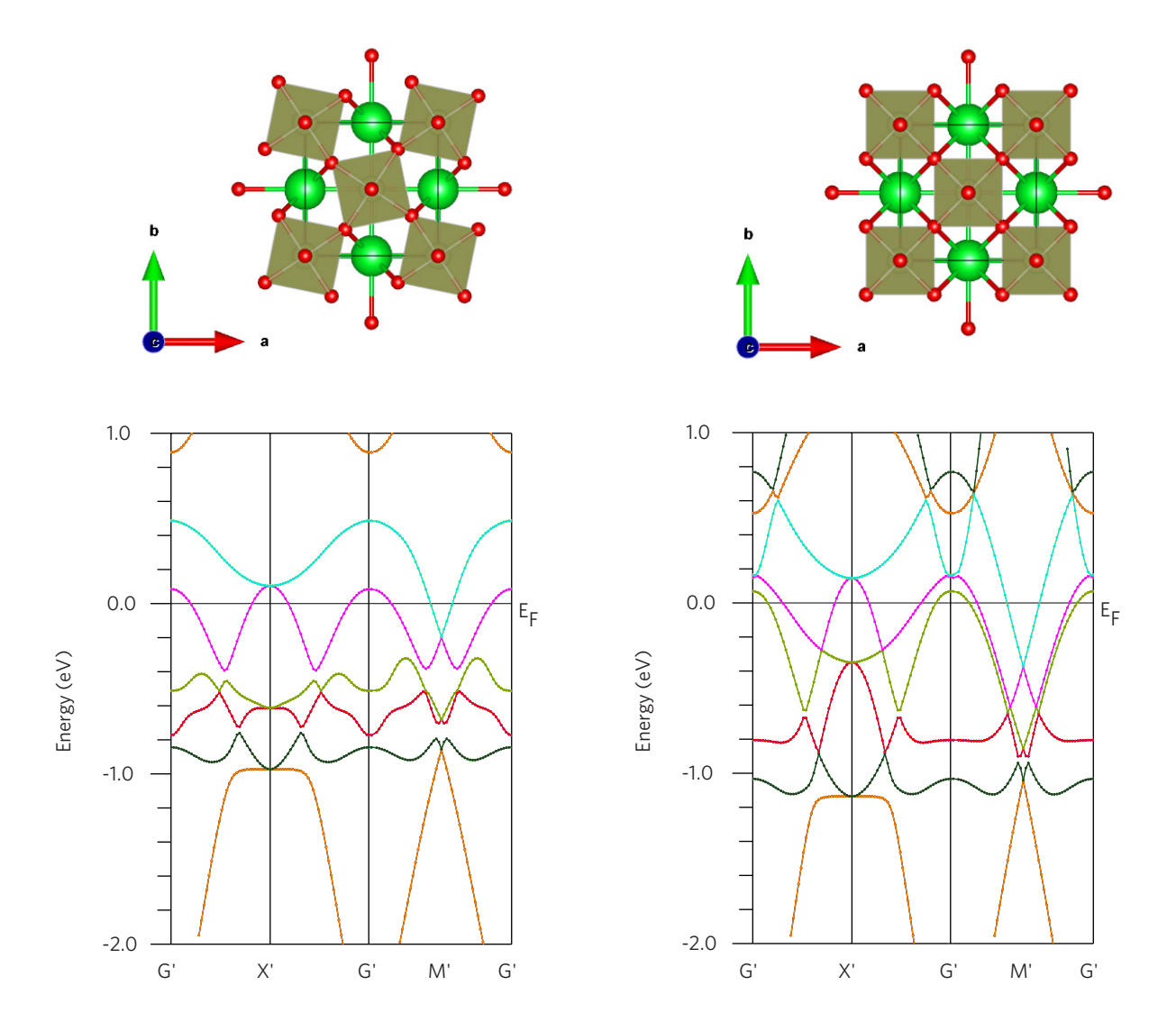


FIG. S2. Band structure of a single layer $\operatorname{Sr_2IrO_4}$ (magnetic space group 81, $P\bar{4}$) in vacuum with and without octahedral rotations. In spite of Ir atoms were initialized with an antiferromagnetic ordering, the final converged solution is non-magnetic at the PBE+SOC level of theory. Note no changes to degeneracy of Ir-d t_{2g} states at X' point (same as M point in the primitive cell) due to octahedral rotations, and no additional bands folded into X' point. See Fig. 5 in the main text for the BZ, and its relation to the primitive cell.